EX-VIVO PORCINE ARTERIAL AND CHORIOALLANTOIC MEMBRANE ACOUSTIC ANGIOGRAPHY USING DUAL FREQUENCY INTRAVASCULAR ULTRASOUND PROBES

K. Heath Martin[1], **Brooks D. Lindsey**[1], **Jianguo Ma**[2], **Timothy C. Nichols**[3], **Xiaoning Jiang**[2], and **Paul A. Dayton**[*,1,4]

[1]Joint Department of Biomedical Engineering, The University of North Carolina and North Carolina State University, Chapel Hill, NC, USA

[2]Department of Mechanical and Aerospace Engineering, North Carolina State University, Raleigh, NC, USA

[3]Department of Pathology and Laboratory Medicine, University of North Carolina, Chapel Hill, NC, USA

[4]Biomedical Research Imaging Center, University of North Carolina, Chapel Hill, NC, USA

Abstract

The presence of blood vessels within a developing atherosclerotic plaque has been shown to be correlated to increased plaque vulnerability and ensuing cardiac events, however, detecting coronary intraplaque neovascularizations poses a significant challenge in the clinic. In this paper, we demonstrate *in vivo* a new intravascular ultrasound imaging method using a dual-frequency transducer to visualize contrast flow in microvessels with high specificity. This method uses a specialized transducer capable of exciting contrast agents at a low frequency (5.5 MHz) while detecting their nonlinear superhamonics at a much higher frequency (37 MHz). *In vitro* evaluation of the approach was performed in a microvascular phantom to produce 3D renderings of simulated vessel patterns and to determine image quality metrics as a function of depth. Furthermore, the ability of the system to detect microvessels is demonstrated both *ex vivo* using porcine arteries and *in vivo* using the chorioallantoic membrane of a developing chicken embryo with optical confirmation. Dual-frequency contrast specific imaging was able to resolve vessels of a similar size to those found in vulnerable atherosclerotic plaques at clinically relevant depths. The results of this study adds growing support for further evaluation and translation of contrast specific imaging in intravascular ultrasound for the detection of vulnerable plaques in atherosclerosis.

Keywords

Ultrasonography; Vasa Vasorum; Dual-Frequency; Superharmonic; Acoustic Angiography; Intravascular Ultrasound; Microbubble; Contrast; Atherosclerosis

---

*Address correspondence to: Paul A Dayton, 304 Taylor Hall, 109 Mason Farm Road, Chapel Hill, NC 27599-6136. padayton@email.unc.edu, Phone: (919) 843-9521.

Introduction

Cardiovascular disease is the leading cause of death globally, responsible for over 17.5 million deaths in 2014 (Mendis 2015). Atherosclerosis is a deadly and progressive disease which initiates with the formation of fatty streaks as the intimal layer of the arterial wall thickens with lipid accumulation (Davies et al. 1988). As lipid-filled macrophages continue to collect, smooth muscle cells within the fatty streak may undergo apoptosis, producing further macrophage accumulation and promoting the transition from fatty streak to atherosclerotic plaque (Kockx et al. 1998). In healthy arterial walls, the outer layers are diffusion-limited and are supplied with nutrients and oxygen by a network of vessels known as the *vasa vasorum* arising in the adventitial layer. As atherosclerotic plaques develop, *vasa vasorum* extend through the media and intimal layers into the plaques themselves (Barger et al. 1984). These intraplaque vessels often have incomplete endothelial linings and lack smooth muscle cell support, making them prone to hemorrhage within the plaque, which is associated with advanced disease progression as the plaque further destabilizes (Virmani et al. 1998; Kolodgie et al. 2003). With additional plaque buildup, a state of arterial stenosis and ischemia develops, which is a more advanced stage of disease commonly associated with increased symptoms and complications (Naghavi et al. 2003). Prior to these observable symptoms, plaque rupture and ensuing cardiac events occur infrequently and seemingly asymptomatically, further obscuring disease progression (Jackson 2011). Intravascular ultrasound (IVUS) screenings are used to quantify disease progression using morphological features such as intima-media thickness (Salonen and Salonen 1993; Amato et al. 2007) or minimum lumen diameter measurements (Abizaid et al. 1999), which aids in designing treatment plans tailored to individuals. Even so, previous studies indicate that a diagnosis based solely on plaque morphology may lack the ability to discern between asymptomatic fibroatheroma and those prone to rupture (Naghavi et al. 2003; Stone et al. 2011). Additionally, histological data has confirmed that vulnerable plaques exhibit enhanced *vasa vasorum* proliferation, intraplaque neovascularizations, or intraplaque hemorrhages (Doyle and Caplice 2007; Mulligan-Kehoe 2010; Schinkel et al. 2010), potentially providing an alternative means for assessing plaque vulnerability through the detection of intraplaque blood flow. Ultrasound contrast agents offer an attractive solution for imaging both morphology and function in assessment of atherosclerosis (Feinstein 2006; Magnoni et al. 2009; ten Kate et al. 2010).

Microbubble contrast agents (MCAs) are micron-sized gas bubbles that provide enhanced acoustic scattering due to the large mismatch in acoustic impedance between the gas core and the surrounding media. MCAs are usually administered in diagnostic procedures to enhance backscatter from blood and aid in identification of blood vessels. Contrast agents have been imaged selectively using IVUS transducers by exploiting their nonlinear behavior through a variety of methods including, but not limited to, pulse inversion (Goertz et al. 2006; Maresca et al. 2013), subharmonic imaging (Goertz et al. 2007), chirp reversal (Maresca et al. 2012; Maresca et al. 2014), and radial modulation (Yu et al. 2014). While some techniques utilize the second harmonic signal, it has been noted that contrast imaging using the second harmonic can be nonspecific to MCAs since tissues also generate second harmonics through nonlinear wave propagation (Thomas and Rubin 1998; Duck 2002;

Goertz et al. 2005). As a result, second harmonic imaging of MCAs can result in loss of specificity in contrast images if measures are not taken to suppress tissue-derived harmonics.

Alternatively, higher order superharmonic imaging of ultrasound contrast agents, defined here as imaging which relies on receiving echoes at frequencies typically 4–6 times higher than the transmitted frequency, provides high resolution and high contrast signal to noise in acquired images. In 2002, Bouakaz *et al* showed that contrast-specific superharmonic imaging produced contrast-to-tissue ratios in excess of 40 dB when using a prototype dual-frequency phased array capable of transmitting at 0.8 MHz and receiving the 3–5th harmonics using elements operating at a center frequency of 2.8 MHz (Bouakaz et al. 2002b). Later, this same approach was extended to a patient study with similar results to demonstrate the feasibility of superharmonic imaging in the clinic (Bouakaz et al. 2003). Images acquired using this contrast imaging method can provide detailed maps of contrast flow in the microvasculature, thus leading to the description 'acoustic angiography' (Gessner et al. 2013). Our group has previously developed single element, dual-frequency (DF) IVUS transducers capable of detecting higher order harmonics to produce images with excellent contrast specificity (Ma et al. 2014) as well as reported transducer and acoustic factors that influence the quality of superharmonic contrast images (Lindsey et al. 2014; Lindsey et al. 2015a; Lindsey et al. 2015b; Ma et al. 2015a). In this article, we present contrast specific *in vivo* superharmonic imaging using custom dual-frequency intravascular (DF-IVUS) transducers. The described experiments evaluate and measure the spatial resolution, sensitivity, and specificity of this intravascular approach for imaging microvessels, in order to establish the feasibility of DF-IVUS superharmonic imaging of intraplaque v*asa vasorum*.

Methods

The Dual-Frequency Probe and Imaging System

Contrast imaging at higher harmonics can be advantageous for achieving higher specificity to contrast agents. Harmonic imaging has typically been performed within the bandwidth of a single transducer, allowing imaging at twice the transmitted frequency at the upper end of the available bandwidth. Contrast imaging at higher harmonics requires transducers with even broader bandwidth. For example, performing 5th harmonic imaging using single element transducers would require a −6 dB fractional bandwidth of at least 133% which is difficult to achieve with piezoelectric materials. However, using multiple elements with separate frequencies allows the transducer to cover a broad range of frequencies to make higher order super-harmonic imaging feasible (Martin et al. 2014). As a result, the study was conducted using a custom 2-element, layered configuration IVUS transducer which has been described previously in detail (Ma et al. 2014; Ma et al. 2015a). Briefly, both elements were composed of lead magnesium niobate-lead titanate (PMN-PT) single crystal with different aperture dimensions oriented in a stacked configuration such that the low frequency element is placed behind the high frequency element.

The transducer forms images of microbubbles selectively by using an unfocused low frequency element (f_c = 5.5 MHz, f_{BW} = 50.0%, 0.6 mm laterally by 3 mm elevationally) to emit excitatory pulses for generating nonlinear echoes from MCAs while the high frequency

element (f_c = 37.2 MHz, f_{BW} = 28.5%, 0.6 mm laterally by 0.5 mm elevationally) detects only the higher harmonics produced by microbubbles. Thus, images formed by operating the transducer in dual-frequency mode will preferentially image nonlinear targets that produce higher order harmonics like MCAs. The two elements are acoustically isolated to prevent undesirable coupling using a frequency selective isolation layer (Azuma et al. 2010; Ma et al. 2015b). Conventional B-mode IVUS imaging was performed for comparison by using the high frequency element in pulse-echo operation.

Signals were acquired from the dual-frequency probe using a custom imaging system capable of volumetric acquisitions (Figure 1). A programmable microcontroller was used to mechanically rotate the probe using a stepper motor having 400 discrete angular positions per revolution (angular step size, θ = 0.9°) and images were acquired at a pulse repetition rate of 100 Hz. The motor and transducer assembly were mounted to a three-axis computer controlled motion stage (Newport XPS, Irvine, CA, USA) which controlled transducer pullback in order to collect images of the entire volume for 3D rendering. The transducer was operated in either DF mode for contrast detection or B-mode for conventional pulse-echo IVUS imaging. In DF mode, the low frequency element was excited using a 5.5 MHz, 50% bandwidth Gaussian enveloped pulse from an arbitrary function generator (AFG3101, Tektronix, Inc., Beaverton, OR, USA). The pulse was amplified to 275 V_{pp} using a 60 dB radiofrequency amplifier (A-500, Electronic Navigation Industries, Rochester, NY, USA) in order to generate 1.2 MPa of peak rarefractional pressure at a depth of 2 mm in water, which was measured using a needle hydrophone (HNA-0400, Onda Corp., Sunnyvale, CA, USA) (Figure 2). The transmission pressure was selected in order to produce detectable nonlinear responses above the 4th harmonic using the high frequency element, similar to reported observations in earlier prototypes (Ma et al. 2014). A beam map of the peak rarefractional pressure from the transmit element was performed by scanning the hydrophone in a water bath using an automated script (Labview, National Instruments, Austin, TX, USA). The received high frequency signal was amplified by 12 dB using a low noise amplifier (BR-640A, Ritec, Warwick, RI, USA) before being digitized at a sampling rate of 100 MHz (PDA14, Signatec, Lockport, IL, USA) for offline post-processing. B-mode imaging was performed using a commercial pulser-receiver (5900PR, Panametrics Inc., Waltham, MA, USA) operating in pulse-echo mode on the high frequency element in order to provide a comparison of imaging modes. Raw signals were first filtered using a zero-phase 8th order Butterworth bandpass filter (33–41 MHz) before being envelope-detected and scan-converted to polar coordinates for display. After image processing each individual slice in the volume (Matlab, The Mathworks, Natick, MA, USA), three-dimensional filtering with a Gaussian kernel (0.59 mm isotropic variance) was applied to smooth the dataset. Finally, the entire volume was then exported to ImageJ (National Institute of Health, Bethesda, MD, USA) where maximum intensity projections were performed to visualize the 3D volume. Statistical significance between computed image metrics were determined with two-sided t-tests at a significance level of $p < 0.05$.

Microbubble Formulation and Preparation

Phospholipid shelled microbubble suspensions were formulated as previously described (Puett et al. 2014) and aliquoted into 3 mL glass vials sealed with a butyl rubber stopper. A

needle was inserted into the headspace of the vial and the gas was exchanged with an inert perfluorocarbon (decafluorobutane, Fluoromed, Round Rock, TX, USA) to form the gaseous core of the MCA. Mechanical agitation using a commercial vial agitator (VialMix, Lantheus Medical Imaging, North Billerica, MA, USA) was performed for 45 s to encapsulate the perfluorocarbon, producing a polydisperse microbubble population. The microbubble population concentration and diameters were measured using a light obscuration and scattering method (AccuSizer 780, Particle Sizing Systems, Santa Barbara, CA, USA). Prepared microbubble populations had a number weighted mean diameter of 1.08 μm measured between 0.5 to 20 μm with 95% of the measured population having a diameter below 1.97 μm. *In vitro* and *ex vivo* contrast experiments were conducted after diluting the stock concentration of microbubbles with distilled water to 10^8 MCA/mL, while *in vivo* experiments used undiluted concentrations of 10^{10} MCA/mL.

Vasa Vasorum Phantom

In vitro phantom experiments were conducted in order to quantify differences between conventional B-mode and contrast specific dual-frequency images of MCAs as a function of depth in an attenuating medium. A gelatin tissue-mimicking phantom using graphite scatterers was made to simulate arterial tissue. The phantom formulation was adapted from a previously described method reported elsewhere (Madsen et al. 1978). Amorphous graphite sized between 0.75–5 μm (Superior Graphite, Chicago, IL, USA) was used to simulate backscattering from tissue and was added at a concentration of 32 mg/mL for attenuation control. Attenuation of the phantom material at applicable frequencies was measured by comparing pressure reduction after inserting phantom material between a piston transducer and hydrophone. Cellulose tubes with an inner diameter of 200 μm were fixed in the phantom material to simulate larger vessels of the *vasa vasorum*. The *vasa vasorum* of human carotid plaques range from 1.6–199.7 μm, with a mean diameter of ~40 μm, while the diameter reported for porcine coronary *vasa vasorum* ranges between 70–160 μm (Kwon et al. 1998; Sluimer and Daemen 2009). In order to determine the imaging metrics as a function of depth, the microcellulose tube was angled relative to the central axis of the vessel lumen so that the amount of phantom material between the contrast-filled vessel and the transducer varied during a volumetric scan (Figure 3). Additional phantoms containing tube networks were fabricated in order to evaluate 3D imaging performance in a more complex environment similar to that encountered *in vivo*. Diluted MCAs were injected into the phantom at a mean velocity of 17.7 mm/s using a calibrated syringe pump (PHD2000, Harvard Apparatus, Holliston, MA, USA). At this rate, the volumetric flow approximates human *in vivo* conditions of a vessel of approximately the same diameter (Riva et al. 1985). The central lumen containing the transducer was 4.5 mm in diameter and filled with distilled water during imaging. This simulates clinical procedures in which a bolus of saline is injected to clear the lumen during the time of imaging to avoid shadowing from microbubble attenuation within the parent artery. The approach is analogous to that described for optical coherence tomography where saline boluses are used during percutaneous interventions to clear red blood cells so that the vessel endothelium may be imaged (Jang et al. 2002; Kubo et al. 2007; Given et al. 2013).

Ex Vivo Porcine Vessel Imaging

While phantoms provide a useful tool for quantifying DF imaging performance under highly controlled conditions, imaging using an *ex vivo* model can be used to test the feasibility of the approach when imaging through arterial tissue. Mesenteric arteries from Rapacz familial hypercholesterolemic pigs (RFH) were used as a surrogate for human arteries, and were donated by the Francis Owens Blood Research Lab (FOBRL, Chapel Hill, NC, USA). RFH pigs are genetically predisposed to develop atheromata at a younger age and these atherosclerotic lesions closely mimic the pathology found in humans. The mutation that results in familial hypercholesterolemia is a missense mutation ($C_{253} \rightarrow T_{253}$) resulting in a transcription substitution ($R_{94} \rightarrow C_{94}$) of a region of the low density lipoprotein receptor that is analogous to exon 4 in the human ligand binding domain (Hasler-Rapacz et al. 1994; Hasler-Rapacz et al. 1998; Grunwald et al. 1999). RFH pigs have been used previously to evaluate contrast enhancement methods for detecting vasa vasorum during the progression of atherosclerosis (Schinkel et al. 2010). All arteries were collected within 1 hour after euthanasia and stored immediately in phosphate buffered saline (PBS) solutions at −20°C until the time of the experiment. Previous work involving human coronary arteries have noted that fixing tissue in formalin significantly alters the acoustic properties of specimens, but freezing and thawing have not produced significant changes in acoustic properties (Gussenhoven et al. 1989; Lockwood et al. 1991). Specimens were thawed, sutured, and attached to a custom fixture to allow the vessel to be stretched to approximately 1.5 times the resected length to approximate *in vivo* conditions (Han and Ku 2001, Figure 4). A 200 μm diameter tube was placed outside the artery to simulate a deep *vasa vasorum* vessel and contrast agents were pumped through the vessel at the same rate used in the phantom study using the same equipment. The artery was submerged in a tank filled with PBS, and both B-mode and DF mode pullbacks were acquired. Arteries collected from 3 different animals were used in this study. All pigs were handled in strict accordance with the USDA regulations and the standards described in the 2011 Guide for the Care and Use of Laboratory Animals (NRC 2011). All procedures and protocols were in accordance with institutional guidelines and approved by the University of North Carolina Institutional Animal Care and Use Committee (IACUC).

Chorioallantoic Membrane *In Vivo* Model

In vivo validations of the approach to selectively image MCAs were performed in developing chicken embryos as a surrogate for *vasa vasorum*. The chorioallantoic membrane (CAM) of developing chicken embryos is composed of a dense capillary network cradled in a sheet of connective tissue and is the primary site for cellular exchange of respiratory gases and metabolic wastes. Due to the low optical scattering of the albumen and the direct visualization of the exposed vasculature, the embryo's developing circulatory system can be imaged and studied optically after removal of the shell. Vessels diameters within the CAM are similar to sizes of human *vasa vasorum* lumens reported previously (43.4 ± 47.4 μm diameters, mean ± s.d.), making it a good model for evaluating the sensitivity of the imaging system to detect small vasculature (Sluimer and Daemen 2009).

Fertilized chicken eggs (broiler line, Ross 708) were collected from a local poultry farm (North Carolina State Chicken Educational Unit, Raleigh, NC, USA) and refrigerated at 6°C

upon arrival for 3–7 days until incubation. Eggs were first incubated *in ovo* at 37.5°C with 70% relative humidity for 3 days, turning every 4 hours using an automated egg rocker (Model 4200/3200, Farm Innovators, Plymouth, IN, USA). Eggs were then cracked and explanted into disposable holders as described by Schomann, et al. (Schomann et al. 2013), and incubated for 14 days in a humidified incubator at 37.5°C, 70% humidity, and 2.0% CO_2 (NAPCO 8000 Series, Thermo Scientific, Waltham, MA, USA). Chicken embryo morphology was classified at the time of imaging according to the Hamburger and Hamilton criteria, with the majority of embryos being classified as HH39-40. The vitelline vein was cannulated to allow the injection of MCAs at a concentration of 10^{10} MCA/mL at a flow rate of 1.0 mL/hr using a syringe pump. A continuous infusion of contrast agents was administered during the entire imaging session. The CAM was prepared for imaging by coupling the transducer to the structure with 37°C phosphate buffered saline.

The intravascular ultrasound probe was positioned adjacent to the CAM and a volumetric acquisition was performed 2 minutes after starting the flow of contrast (Figure 5). Image slices orthogonal to the direction of transducer pullback were acquired at 200 μm intervals while operating in DF mode for contrast specific imaging. Conventional B-mode and DF mode volumetric scans were acquired both before and after administration of MCAs for comparison. Additionally, contrast infusion was monitored by acquiring volume scans in DF mode at 2 minute intervals for a total 12 minutes. Photographs of the CAM corresponding to the region that was scanned were taken to provide an optical reference to measure vessel diameters. 11 embryos were imaged. Photographs were analyzed in ImageJ to measure the width of the vessels within the imaging region.

Results

Field Profile During Transmission and Received Spectra from MCA

The transmission profile of the low frequency element was recorded using a needle hydrophone positioned in a water bath in order to determine spatial variation of the excitatory signal for the custom IVUS transducer. The 5.5 MHz element was capable of producing 1.2 MPa on-axis at a range of 2 mm from the surface of the transducer (Figure 6). Hydrophone measurements indicate that the beam remained collimated at a depth of 7.4 mm where the pressure dropped −6 dB relative to the peak (600 kPa). Field II (Jensen and Svendsen 1992; Jensen 1996) was used to simulate the pressure field produced by the low frequency element to compare the measured field to ideal results (Figure 6b). While simulated and measured results show good agreement, some off-axis energy deposition occurs that was not predicted by the simulation. However, these off-axis energy levels are located at angles where the receive element is highly insensitive making undesirable effects, such as clutter, which is less of an issue when operating in DF mode. For reference, a contour is drawn in Figure 6 to approximate the region of highest microbubble destruction and loss of echogenicity where the transmitted waveform exceeds a mechanical index (MI) of 0.20. This MI corresponds to the microbubble fragmentation threshold for the type of microbubbles used in this study (Lindsey et al. 2015a).

Three Dimensional Renderings of Microvascular Phantoms

Three dimensional imaging was performed on several phantoms in order to compare B-mode with DF mode contrast imaging (Figure 7). Conventional B-mode images were unable to differentiate contrast-enhanced microvessels from surrounding phantom tissue. In comparison, DF images were highly selective to detecting signal only from regions containing contrast agents. In light of these results, quantitative image analysis was performed as a function of depth into tissue for both B-mode and DF mode operation of this transducer.

IVUS pullbacks were performed using a 200 μm diameter tube embedded in a graphite phantom at varying depths. Prior to contrast administration, baseline scans of both imaging modes were performed to provide a reference point for imaging improvement after MCAs were added. Contrast-to-noise ratios (CNR), contrast-to-tissue ratios (CTR), and tissue-to-noise ratios (TNR) were calculated from images by segmenting regions of interest (ROI) corresponding to MCAs for contrast measurements, water for noise measurements, or phantom material for tissue measurements (Goertz et al. 2007). Power estimates from these regions were calculated from the square of the radio-frequency (RF) lines. Because of the radial symmetry of our phantoms, ROIs were rotated about the transducer to ensure the compared locations were calculated at the same depths using the same number of pixels to calculate the average (Figure 8). Centroids of the ROIs were calculated and used to determine the radial distance from the aperture of the transducer. Results of the analysis were grouped according to distance with bin sizes of 1.5 mm ranging from 2.5 to 10 mm. Student's t-tests ($\alpha = 0.05$) show that CNR was non-zero for both imaging modes at depths below 7.0 mm. Paired testing between the imaging modes indicate that B-mode images had a statistically higher CNR (7.36 vs 2.35 dB at 3.25 mm), however, CTR and TNR calculations suggest that this enhancement is not specific to MCAs alone. At all tested depths, B-mode CTR was statistically zero while DF images had non-zero CTRs of 1.00 dB at 6.25 mm and up to 1.75 dB at 4.75 mm. CTR values using DF images were fundamentally limited by low CNR of the imaging system in that received contrast signal was very close to the noise floor, diminishing the potential for higher values of CTR. Lower values of CTR are accompanied by higher specificity to contrast signal in images which can be observed when evaluating the differences in TNR. The TNR of B-mode images at depths below 7.0 mm were non-zero and statistically higher than DF images which averaged 0.47 dB through depth. As a result, DF images using higher order superharmonics produce images with excellent tissue suppression within physiologically relevant depths for IVUS imaging.

The axial and lateral size of the 200 μm diameter tube was measured from processed DF mode images after administration of contrast agents. Tube measurements were calculated as the full-width half maximum of the tube region relative to the background noise level in a phantom. Using this method, the axial measurement of the tube was 704.0 ± 24.6 μm (mean ± s.e) while the lateral measurement was 510.5 ± 19.4 μm at an average depth of 4 mm in tissue.

Ex Vivo Contrast Detection in Arteries from RFH Pigs

Preliminary results indicate that imaging through the arterial wall can be accomplished in mesenteric arteries. Coregistered B-mode and DF mode contrast specific images of an example specimen are given in Figure 9 along with CTR. Contrast to tissue ratios were calculated using the ROI approach described previously with tissue ROIs enclosing the B-mode vessel structure through all slices in the volumetric set. Prior to injection of contrast agents, a B-mode scan was gathered and used to locate the front and back boundaries of the cellulose tube to accurately define contrast signal ROIs for subsequent scans (Figure 9a). In DF mode, the microcellulose tube could be clearly located with excellent tissue suppression (Figure 9b). Acoustic backscattering intensity from tissue was higher than that from microbubbles at the fundamental frequency (37 MHz), resulting in negative *ex vivo* B-mode CTR while DF mode CTR remained positive. Combining the DF and B-mode images provides both morphology of the vessel typically found in IVUS with contrast detection of microvascular flow (Figure 9c–d). These *ex vivo* studies demonstrate that higher order superharmonic signals from contrast agents can be generated using a low frequency element and detected using a high frequency receiving element through excised porcine arteries, suggesting that penetration through similar tissues should also be feasible *in vivo*.

In Vivo Contrast Detection of Microvascular Flow

Translation of this technique into the *in vivo* environment was performed after establishing feasibility from *in vitro* experiments. Photographs were taken of the chicken embryo to provide optical verification of vascular structures after embryos were cannulated for vascular perfusion of contrast agents (Figure 10a). Three-dimensional renderings of vessel networks were visualized by performing maximum intensity projections on volumetric datasets (Figure 10b). Contrast flow was monitored over time as a continuous infusion of contrast agents was administered while acquiring DF volumetric pullbacks. Contrast enhancement (CE), defined as the signal increase from pre-injection values, was calculated and used as a surrogate for CTR while CNR was computed as described previously. Since tissue devoid of contrast agents was not realizable in this animal model, the method of calculating the TNR *in vivo* was estimated by taking the ratio of CNR to CE. This method of calculation relies on the assumption that CE behaves similarly to CTR since TNR can be computed from the ratio of CNR to CTR. Image metrics were calculated and plotted over time for comparison (Figure 10c–d).

As seen in the phantom case, B-mode images had a non-zero CNR prior to contrast administration (6.42 dB) resulting from tissue backscatter from vessel walls. Dual-frequency mode images started with a statistically zero CNR ($p = 0.28$) but improved to a maximum value of 3.49 dB after 6 minutes of infusion. The slightly negative slope over time observed in DF mode CNR is likely to be a result of decreased cardiac function of the embryo. Contrast enhancement for B-mode was greater than DF mode (4.34 vs 2.30 dB) at the end time point, however, the difference was not statistically significant ($p = 0.071$). Tissue-to-noise ratio was computed to determine the ability of the imaging mode to be specific to contrast agents. The TNR for DF images was statistically zero for all time points recorded while B-mode images had a mean TNR of 6.66 dB.

Axial and lateral resolution was computed in optical and DF contrast images of the CAM vasculature. Optical measurements of vessels were taken such that they would correspond to lateral measurements in DF images and it was assumed that the diameter of the vessel in this plane would also be the diameter in the axial direction. The smallest vessel detected *in vivo* was measured to have a diameter of 140 ± 8.1 μm (mean ± s.e.) optically while the DF image measured 626.5 ± 16.9 μm axially and 603.2 ± 22.6 μm laterally.

Discussion

Our study has demonstrated that imaging using an IVUS transducer with an exceptionally large bandwidth achieved through multiple elements of different frequency ranges produces images with sensitivity to contrast in the microvasculature and tissue suppression not possible with standard single frequency IVUS probes. Superharmonic contrast images have reduced tissue contamination because the amplitude of the signal emitted by MCAs is much higher than that produced by tissue at frequencies 3 to 5 times higher than the transmitted frequency (Bouakaz et al. 2002a). While increasing tissue suppression in contrast images is beneficial, the contrast signal-to-noise ratio using higher order harmonics is reduced compared to using lower harmonics such as the 2nd or 3rd harmonics and provides a significant challenge to this approach using single element transducers. The peak CTR from the phantom study (1.75 dB) was approximately the same as the measured CNR, implying that contrast images were specific to MCAs alone. However, other studies of contrast-enhanced IVUS have reported higher values for CNR (approximately 30 dB, 20 dB, and 20 dB for sub-, ultra-, and superharmonic, respectively) than those presented here, though it is difficult to draw a direct comparison since imaging depths, vessel diameter, and type of contrast agents used are not the same (Goertz et al. 2006; Goertz et al. 2007; Maresca et al. 2013). This imaging approach would likely benefit from translation to circular arrays where post-processing approaches such as beamforming on either transmit or receive would help improve the CNR over what can be obtained using only a single element.

The moderate mechanical indices used for causing broadband excitation of contrast agents disrupts the shell of the microbubbles and can lower the echogenicity of contrast agents upon further insonation (Chomas et al. 2001; Lindsey et al. 2015a). Replenishment of the contrast agents with blood flow allows echogenicity to recover over time making this issue less prevalent in larger diameter vessels which have higher volumetric flow rates, but may impact how well smaller vessels are resolved. *In vivo* measurements have indicated that vessels of 140 μm in diameter may be the limit of detection with the current imaging system, but it is unclear whether this limit is imposed by reduced cross-sectional backscatter or by contrast destruction and replenishment rates.

While off-axis energy deposition is normally avoided in ultrasound imaging to reduce clutter (Pinton et al. 2011), an added consequence when imaging contrast agents is to prevent the destruction of contrast agents. In Figure 6, the measured transmit pressure field of our transducer exhibited some off-axis energy deposition in the near field, which could potentially destroy contrast agents before being imaged by the receiving element, thus reducing CNR. However, this effect was not significant enough to prevent full 3D reconstructions of vascular phantoms. A 200 μm diameter vessel could be resolved in a

tissue mimicking phantom at depths up to 7 mm deep without the aid of signal averaging or use of multiple pulses.

Traditional B-mode IVUS images typically have greater axial resolution rather than lateral resolution since they use higher frequencies with small aperture transducers on both transmission and reception. However, axial resolution in contrast specific images using the described dual-frequency transducer was on average lower than the lateral resolution even though B-mode images using the high frequency element were able to resolve structures smaller than 200 μm axially. These observations provide growing support that axial resolution is degraded in DF operation primarily due to the increased pulse length used on transmission as observed previously (Ma et al. 2014), while lateral resolution was primarily dependent upon wave diffraction of the receiving element, but further analysis would be required to determine the validity of this hypothesis.

The *ex vivo* studies demonstrated that DF contrast specific imaging could detect the presence of a 200 μm diameter tube located outside of an excised porcine artery. Detection of microvascular flow external to the adventitial layer of the vessel is important since most *vasa vasorum* are externally derived and this location would be more difficult to detect due increased depth and attenuation. DF mode CTR increases at shallower depths suggesting that if vascular flow external to the vessel can be detected, the neovascularizations occurring in fatty plaques at reduced depths would likely be detectable as well. The low number of animals used in this study prevents statistical analysis.

At frequencies relevant for IVUS imaging, blood scattering effects become significant and attenuation becomes more severe (Lockwood et al. 1991). Additionally, the presence of MCAs in the lumen of the vessel where the IVUS catheter is placed results in attenuation and nonlinear propagation effects, which can produce pseudoenhancement artifacts, or contrast signal where no MCAs are present (Tang and Eckersley 2006; ten Kate et al. 2012). This artifact may mask the presence of true contrast in IVUS if vessels supplying the lesion lie close to the lumen of the parent artery. The experiments presented in this work represent a scenario in which the majority of microbubbles have been cleared by either temporary balloon occlusion or a saline flush to clear blood flow in the main artery while collecting an image (Jang et al. 2002). The studies presented reflect the saline flush case; it should be noted that the results would be subject to more severe attenuation if red blood cells and MCAs fill the vessel lumen during imaging.

Microvascular networks of the galline chorioallantoic membrane were imaged and rendered. Dual-frequency contrast images were highly selective to imaging only contrast signal and had a TNR of zero for all time points. Contrast signal-to-noise ratios were higher in B-mode images compared to DF images in both *in vitro* and *in vivo* trials, but B-mode images had a CNR that was non-zero even though contrast agents had not yet been injected (Figure 10c) indicating that this signal was not from contrast agents but rather vascular tissue within the region of interest. Fundamentally, the CNR of the imaging system limits the CTR that can be acquired, producing CTR values that were nearly equivalent to CNR when operating in DF mode.

Conclusions

A new intravascular ultrasound method for visualizing microbubble contrast agents using higher order superharmonics has been described and demonstrated to detect microvascular blood vessels *in vivo*. Dual-frequency images effectively suppress tissue signal, but have lower signal-to-noise ratios than other contrast specific imaging methods. However, contrast images obtained using this method reject tissue well, making it suitable for producing 3D renderings of vessels. This technique has demonstrated its ability to detect contrast in 200 μm vessels *ex vivo* using porcine arteries and vessels smaller than 200 μm in diameter *in vivo* without using multiple pulses. Additionally, phantom studies have demonstrated the feasibility of a dual-frequency approach to detect *vasa vasorum*-sized vessels at depths up to 7 mm.

Acknowledgments

References

Abizaid AS, Mintz GS, Abizaid A, Mehran R, Lansky AJ, Pichard AD, Satler LF, Wu H, Kent KM, Leon MB. One-year follow-up after intravascular ultrasound assessment of moderate left main coronary artery disease in patients with ambiguous angiograms. J Am Coll Cardiol. 1999; 34:707–15. [PubMed: 10483951]

Amato M, Montorsi P, Ravani A, Oldani E, Galli S, Ravagnani PM, Tremoli E, Baldassarre D. Carotid intima-media thickness by B-mode ultrasound as surrogate of coronary atherosclerosis: Correlation with quantitative coronary angiography and coronary intravascular ultrasound findings. Eur Heart J. 2007; 28:2094–101. [PubMed: 17597051]

Azuma T, Ogihara M, Kubota J, Sasaki A, Umemura S, Furuhata H. Dual-frequency ultrasound imaging and therapeutic bilaminar array using frequency selective isolation layer. IEEE Trans Ultrason Ferroelectr Freq Control. 2010; 57:1211–24. [PubMed: 20442033]

Barger AC, Beeuwkes R, Lainey LL, Silverman KJ. Hypothesis: vasa vasorum and neovascularization of human coronary arteries. A possible role in the pathophysiology of atherosclerosis. N Engl J Med. 1984; 310:175–7. [PubMed: 6197652]

Bouakaz A, Frigstad S, ten Cate FJ, de Jong N. Improved contrast to tissue ratio at higher harmonics. Ultrasonics. 2002a; 40:575–8. [PubMed: 12160004]

Bouakaz A, Frigstad S, ten Cate FJ, de Jong N. Super harmonic imaging: a new imaging technique for improved contrast detection. Ultrasound Med Biol. 2002b; 28:59–68. [PubMed: 11879953]

Bouakaz A, Krenning BJ, Vletter WB, ten Cate FJ, de Jong N. Contrast superharmonic imaging: A feasibility study. Ultrasound Med Biol. 2003; 29:547–53. [PubMed: 12749924]

Chomas JE, Dayton PA, Allen J, Morgan K, Ferrara KW. Mechanisms of contrast agent destruction. IEEE Trans Ultrason Ferroelectr Freq Control. 2001; 48:232–48. [PubMed: 11367791]

Davies MJ, Woolf N, Rowles PM, Pepper J. Morphology of the endothelium over atherosclerotic plaques in human coronary arteries. Br Heart J. 1988; 60:459–64. [PubMed: 3066389]

Doyle B, Caplice N. Plaque neovascularization and antiangiogenic therapy for atherosclerosis. J Am Coll Cardiol. 2007; 49:2073–80. [PubMed: 17531655]

Duck FA. Nonlinear acoustics in diagnostic ultrasound. Ultrasound Med Biol. 2002; 28:1–18. [PubMed: 11879947]

Feinstein SB. Contrast ultrasound imaging of the carotid artery vasa vasorum and atherosclerotic plaque neovascularization. J Am Coll Cardiol. 2006; 48:236–43. [PubMed: 16843169]

Gessner R, Frederick CB, Foster FS, Dayton PA. Acoustic angiography: a new imaging modality for assessing microvasculature architecture. Int J Biomed Imaging. 2013; 2013:936593. [PubMed: 23997762]

Given CA, Attizzani GF, Jones MR, Ramsey CN, Brooks WH, Costa MA, Bezerra HG. Frequency-domain optical coherence tomography assessment of human carotid atherosclerosis using saline flush for blood clearance without balloon occlusion. AJNR American journal of neuroradiology. 2013; 34:1414–8. [PubMed: 23391841]

Goertz DE, Cherin E, Needles A, Karshafian R, Brown AS, Burns PN, Foster FS. High frequency nonlinear B-scan imaging of microbubble contrast agents. IEEE Trans Ultrason Ferroelectr Freq Control. 2005; 52:65–79. [PubMed: 15742563]

Goertz DE, Frijlink ME, de Jong N, van der Steen AFW. Nonlinear intravascular ultrasound contrast imaging. Ultrasound Med Biol. 2006; 32:491–502. [PubMed: 16616596]

Goertz DE, Frijlink ME, Tempel D, Bhagwandas V, Gisolf A, Krams R, de Jong N, van der Steen AFW. Subharmonic contrast intravascular ultrasound for vasa vasorum imaging. Ultrasound Med Biol. 2007; 33:1859–72. [PubMed: 17683850]

Grunwald KA, Schueler K, Uelmen PJ, Lipton BA, Kaiser M, Buhman K, Attie AD. Identification of a novel Arg-->Cys mutation in the LDL receptor that contributes to spontaneous hypercholesterolemia in pigs. Journal of lipid research. 1999; 40:475–85. [PubMed: 10064736]

Gussenhoven EJ, Essed CE, Lancée CT, Mastik F, Frietman P, van Egmond FC, Reiber J, Bosch H, van Urk H, Roelandt J, Bom N. Arterial wall characteristics determined by intravascular ultrasound imaging: An in vitro study. J Am Coll Cardiol. 1989; 14:947–52. [PubMed: 2677088]

Han H-C, Ku DN. Contractile responses in arteries subjected to hypertensive pressure in seven-day organ culture. Ann of Biomed Eng. 2001; 29:467–75. [PubMed: 11459340]

Hasler-Rapacz J, Ellegren H, Fridolfsson AK, Kirkpatrick B, Kirk S, Andersson L, Rapacz J. Identification of a mutation in the low density lipoprotein receptor gene associated with recessive familial hypercholesterolemia in swine. American journal of medical genetics. 1998; 76:379–86. [PubMed: 9556295]

Hasler-Rapacz JO, Nichols TC, Griggs TR, Bellinger DA, Rapacz J. Familial and diet-induced hypercholesterolemia in swine. Lipid, ApoB, and ApoA-I concentrations and distributions in plasma and lipoprotein subfractions. Arteriosclerosis and thrombosis : a journal of vascular biology / American Heart Association. 1994; 14:923–30.

Jackson SP. Arterial thrombosis-insidious, unpredictable and deadly. Nat Med. 2011; 17:1423–36. [PubMed: 22064432]

Jang I-K, Bouma BE, Kang D-H, Park S-J, Park S-W, Seung K-B, Choi K-B, Shishkov M, Schlendorf K, Pomerantsev E, Houser SL, Aretz HT, Tearney GJ. Visualization of coronary atherosclerotic plaques in patients using optical coherence tomography: comparison with intravascular ultrasound. J Am Coll Cardiol. 2002; 39:604–9. [PubMed: 11849858]

Jensen JA. Field: A program for simulating ultrasound systems. Paper presented at the 10th Nordic-Baltic Conference on Biomedical Imaging. Published in Medical & Biological Engineering & Computing. 1996; 351:3.

Jensen JA, Svendsen NB. Calculation of pressure fields from arbitrarily shaped, apodized, and excited ultrasound transducers. IEEE Trans Ultrason Ferroelectr Freq Control. 1992; 39:262–7. [PubMed: 18263145]

Kockx MM, De Meyer GR, Muhring J, Jacob W, Bult H, Herman AG. Apoptosis and related proteins in different stages of human atherosclerotic plaques. Circulation. 1998; 97:2307–15. [PubMed: 9639374]

Kolodgie FD, Gold HK, Burke AP, Fowler DR, Kruth HS, Weber DK, Farb A, Guerrero LJ, Hayase M, Kutys R, Narula J, Finn AV, Virmani R. Intraplaque hemorrhage and progression of coronary atheroma. N Engl J Med. 2003; 349:2316–25. [PubMed: 14668457]

Kubo T, Imanishi T, Takarada S, Kuroi A, Ueno S, Yamano T, Tanimoto T, Matsuo Y, Masho T, Kitabata H, Tsuda K, Tomobuchi Y, Akasaka T. Assessment of Culprit Lesion Morphology in Acute Myocardial Infarction. J Am Coll Cardiol. 2007; 50:933–9. [PubMed: 17765119]

Kwon HM, Sangiorgi G, Ritman EL, Lerman A, McKenna C, Virmani R, Edwards WD, Holmes DR, Schwartz RS. Adventitial vasa vasorum in balloon-injured coronary arteries: visualization and

quantitation by a microscopic three-dimensional computed tomography technique. J Am Coll Cardiol. 1998; 32:2072–9. [PubMed: 9857895]

Lindsey BD, Rojas JD, Dayton PA. On the relationship between microbubble fragmentation, deflation and broadband superharmonic signal production. Ultrasound Med Biol. 2015a; 41:1711–25. [PubMed: 25766572]

Lindsey BD, Rojas JD, Martin KH, Shelton S, Dayton PA. Acoustic characterization of contrast-to-tissue ratio and axial resolution for dual-frequency contrast-specific acoustic angiography imaging. IEEE Trans Ultrason Ferroelectr Freq Control. 2014; 61:1668–87. [PubMed: 25265176]

Lindsey BD, Shelton SS, Dayton PA. Optimization of contrast-to-tissue ratio through pulse windowing in dual-frequency "acoustic angiography" imaging. Ultrasound Med Biol. 2015b

Lockwood GR, Ryan LK, Hunt JW, Foster FS. Measurement of the ultrasonic properties of vascular tissues and blood from 35–65 MHz. Ultrasound Med Biol. 1991; 17:653–66. [PubMed: 1781068]

Ma J, Martin KH, Dayton PA, Jiang X. A preliminary engineering design of intravascular dual-frequency transducers for contrast-enhanced acoustic angiography and molecular imaging. IEEE Trans Ultrason Ferroelectr Freq Control. 2014; 61:870–80. [PubMed: 24801226]

Ma J, Martin KH, Li Y, Dayton PA, Shung KK, Zhou Q, Jiang X. Design factors of intravascular dual frequency transducers for super-harmonic contrast imaging and acoustic angiography. Phys Med Biol. 2015a; 60:3441–57. [PubMed: 25856384]

Ma J, Steer MB, Jiang X. An acoustic filter based on layered structure. Appl Phys Lett. 2015b; 106:111903. [PubMed: 25829548]

Madsen EL, Zagzebski JA, Banjavie RA, Jutila RE. Tissue mimicking materials for ultrasound phantoms. Med Phys. 1978; 5:391–4. [PubMed: 713972]

Magnoni M, Coli S, Marrocco-Trischitta MM, Melisurgo G, De Dominicis D, Cianflone D, Chiesa R, Feinstein SB, Maseri A. Contrast-enhanced ultrasound imaging of periadventitial vasa vasorum in human carotid arteries. Eur J Echocardiogr. 2009; 10:260–4. [PubMed: 18757860]

Maresca D, Jansen K, Renaud G, van Soest G, Li X, Zhou Q, de Jong N, Shung KK, van der Steen AFW. Intravascular ultrasound chirp imaging. Appl Phys Lett. 2012; 100:043703.

Maresca D, Renaud G, van Soest G, Li X, Zhou Q, Shung KK, de Jong N, van der Steen AFW. Contrast-enhanced intravascular ultrasound pulse sequences for bandwidth-limited transducers. Ultrasound Med Biol. 2013; 39:706–13. [PubMed: 23384459]

Maresca D, Skachkov I, Renaud G, Jansen K, van Soest G, de Jong N, van der Steen AFW. Imaging microvasculature with contrast-enhanced ultraharmonic ultrasound. Ultrasound Med Biol. 2014; 40:1318–28. [PubMed: 24613639]

Martin KH, Lindsey BD, Ma J, Lee M, Li S, Foster FS, Jiang X, Dayton PA. Dual-frequency piezoelectric transducers for contrast enhanced ultrasound imaging. Sensors. 2014; 14:20825–42. [PubMed: 25375755]

Mendis, S. Global status report on noncommunicable diseases 2014. Geneva: World Health Organization; 2015.

Mulligan-Kehoe MJ. The vasa vasorum in diseased and nondiseased arteries. Am J Physiol Heart Circ Physiol. 2010; 298:H295–305. [PubMed: 19940078]

Naghavi M, Libby P, Falk E, Casscells SW, Litovsky S, Rumberger J, Badimon JJ, Stefanadis C, Moreno P, Pasterkamp G, Fayad Z, Stone PH, Waxman S, Raggi P, Madjid M, Zarrabi A, Burke A, Yuan C, Fitzgerald PJ, Siscovick DS, de Korte CL, Aikawa M, Juhani Airaksinen KE, Assmann G, Becker CR, Chesebro JH, Farb A, Galis ZS, Jackson C, Jang I-K, Koenig W, Lodder Ra, March K, Demirovic J, Navab M, Priori SG, Rekhter MD, Bahr R, Grundy SM, Mehran R, Colombo A, Boerwinkle E, Ballantyne C, Insull W, Schwartz RS, Vogel R, Serruys PW, Hansson GK, Faxon DP, Kaul S, Drexler H, Greenland P, Muller JE, Virmani R, Ridker PM, Zipes DP, Shah PK, Willerson JT. From vulnerable plaque to vulnerable patient: a call for new definitions and risk assessment strategies: Part I. Circulation. 2003; 108:1664–72. [PubMed: 14530185]

NRC. Guide for the Care and Use of Laboratory Animals: Eighth Edition. Washington, DC: The National Academies Press; 2011. Committee for the Update of the Guide for the Care and Use of Laboratory Animals.

Pinton G, Trahey GE, Dahl J. Sources of image degradation in fundamental and harmonic ultrasound imaging using nonlinear, full-wave simulations. IEEE Trans Ultrason Ferroelectr Freq Control. 2011; 58:754–65. [PubMed: 21507753]

Puett C, Sheeran PS, Rojas JD, Dayton PA. Pulse sequences for uniform perfluorocarbon droplet vaporization and ultrasound imaging. Ultrasonics. 2014; 54:2024–33. [PubMed: 24965563]

Riva CE, Grunwald JE, Sinclair SH, Petrig BL. Blood velocity and volumetric flow rate in human retinal vessels. Invest Ophthalmol Vis Sci. 1985; 26:1124–32. [PubMed: 4019103]

Salonen JT, Salonen R. Ultrasound B-mode imaging in observational studies of atherosclerotic progression. Circulation. 1993; 87:II56–65. [PubMed: 8443925]

Schinkel AFL, Krueger CG, Tellez A, Granada JF, Reed JD, Hall A, Zang W, Owens C, Kaluza GL, Staub D, Coll B, ten Cate FJ, Feinstein SB. Contrast-enhanced ultrasound for imaging vasa vasorum: comparison with histopathology in a swine model of atherosclerosis. Eur J Echocardiogr. 2010; 11:659–64. [PubMed: 20385655]

Schomann T, Qunneis F, Widera D, Kaltschmidt C, Kaltschmidt B. Improved method for ex ovo-cultivation of developing chicken embryos for human stem cell xenografts. Stem Cells Int. 2013; 960958:1–9.

Sluimer JC, Daemen MJ. Novel concepts in atherogenesis: angiogenesis and hypoxia in atherosclerosis. J Pathol. 2009; 218:7–29. [PubMed: 19309025]

Stone GW, Maehara A, Lansky AJ, de Bruyne B, Cristea E, Mintz GS, Mehran R, McPherson J, Farhat N, Marso SP, Parise H, Templin B, White R, Zhang Z, Serruys PW. A prospective natural-history study of coronary atherosclerosis. N Engl J Med. 2011; 364:226–35. [PubMed: 21247313]

Tang M-X, Eckersley RJ. Nonlinear propagation of ultrasound through microbubble contrast agents and implications for imaging. IEEE Trans Ultrason Ferroelectr Freq Control. 2006; 53:2406–15. [PubMed: 17186923]

ten Kate GL, Renaud GGJ, Akkus Z, van den Oord SCH, ten Cate FJ, Shamdasani V, Entrekin RR, Sijbrands EJG, de Jong N, Bosch JG, Schinkel AFL, van der Steen AFW. Far-wall pseudoenhancement during contrast-enhanced ultrasound of the carotid arteries: clinical description and in vitro reproduction. Ultrasound Med Biol. 2012; 38:593–600. [PubMed: 22341054]

ten Kate GL, Sijbrands EJG, Valkema R, ten Cate FJ, Feinstein SB, van der Steen AFW, Daemen MJ, Schinkel AFL. Molecular imaging of inflammation and intraplaque vasa vasorum: a step forward to identification of vulnerable plaques? J Nucl Cardiol. 2010; 17:897–912. [PubMed: 20552308]

Thomas JD, Rubin DN. Tissue harmonic imaging: why does it work? J Am Soc Echocardiogr. 1998; 11:803–8. [PubMed: 9719092]

Virmani R, Narula J, Farb A. When neoangiogenesis ricochets. American Heart Journal. 1998; 136:937–9. [PubMed: 9842001]

Yu F, Villanueva F, Chen X. Radial modulation contrast imaging using a 20-MHz single-element intravascular ultrasound catheter. IEEE Trans Ultrason Ferroelectr Freq Control. 2014; 61:779–91. [PubMed: 24803134]
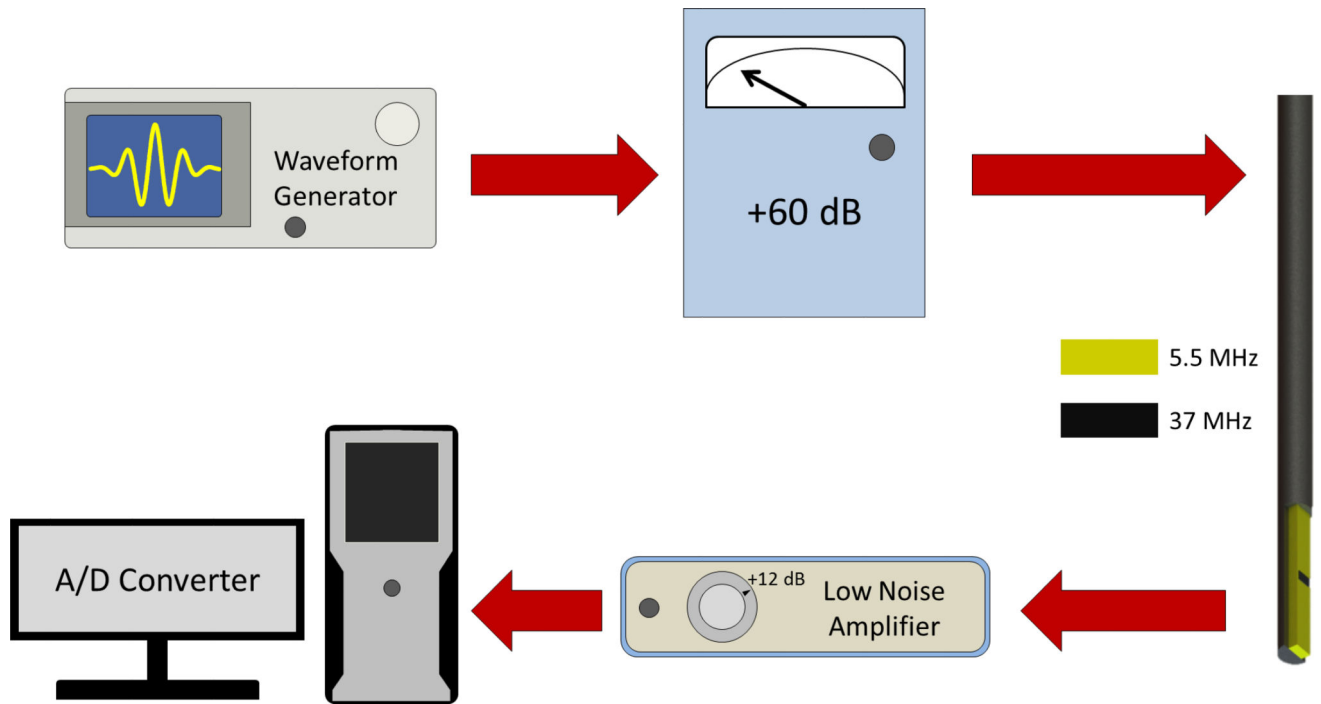
Figure 1.
Data and control signal flow for acquiring superharmonic signals using the dual-frequency transducer.
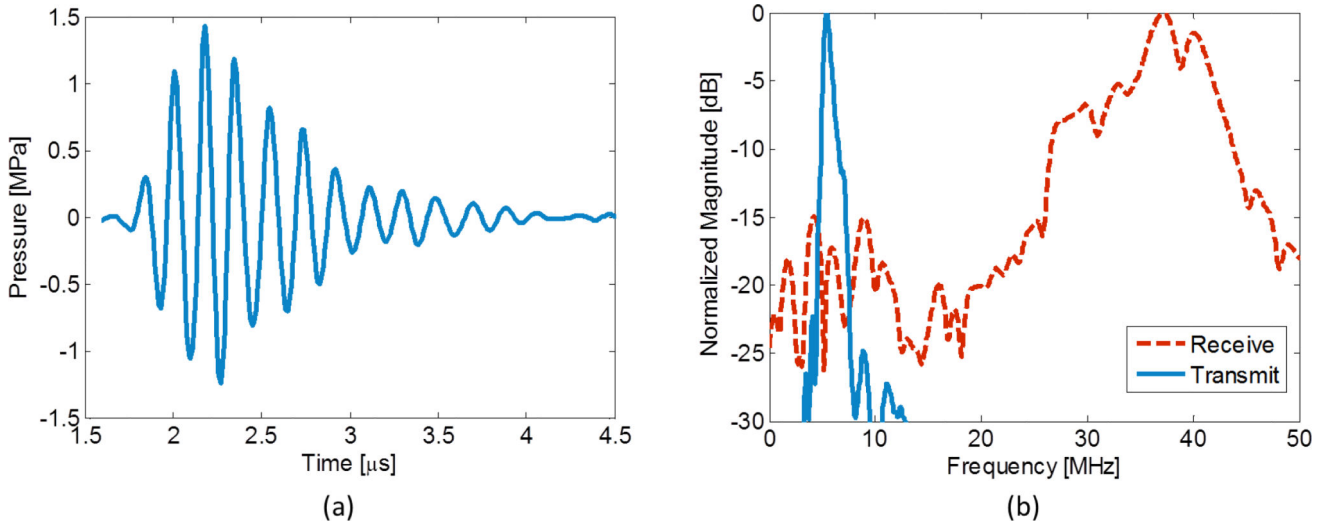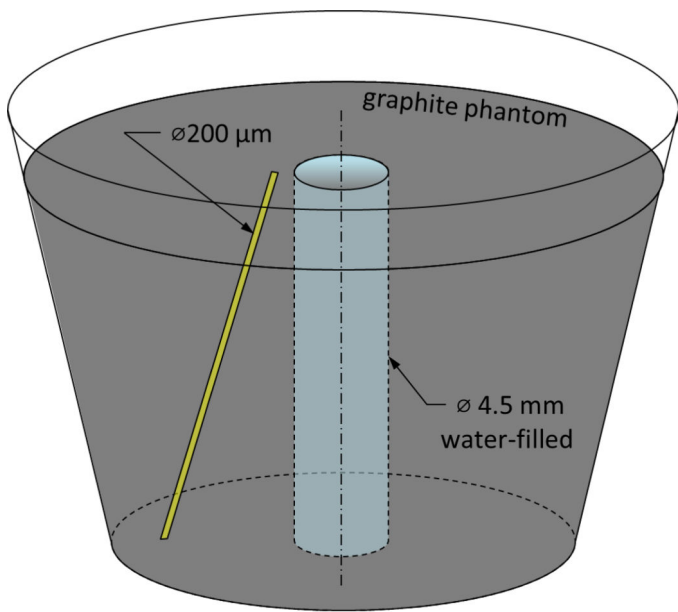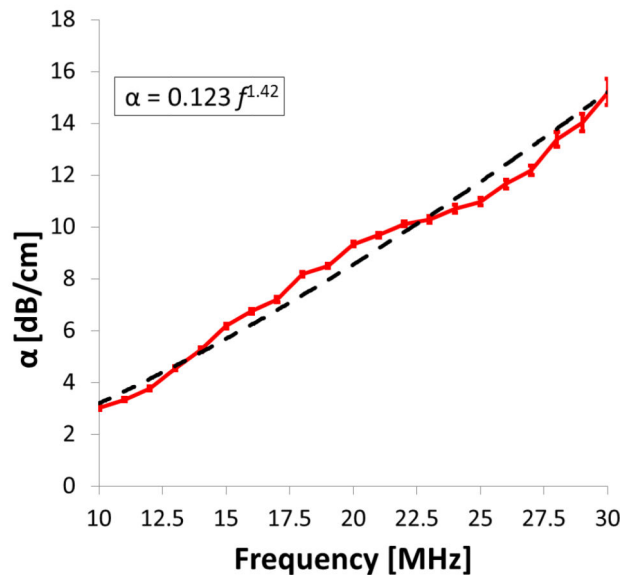
Figure 2.
Transmission and reception characteristics of the dual-frequency IVUS probe. (a) The time-varying pressure produced by the 5.5 MHz element that was used when the transducer was operated in DF mode. The pressure response was recorded using a calibrated hydrophone in water at a depth of 2 mm. (b) The normalized power spectra of the transmitted pulse and the receiving element impulse response. There is little overlap between transmission and reception spectra, indicating that received signals will primarily consist of nonlinear harmonics.

Figure 3.
(a) Schematic of the microvascular phantom used to simulate *vasa vasorum* embedded in tissue. A 200 μm diameter cellulose tube was used to simulate a microvascular channel of the *vasa vasorum* within the tissue. (b) Frequency-dependent attenuation of the graphite phantom. The speed of sound measured to be 1548 ± 44 m/s at 22°C.
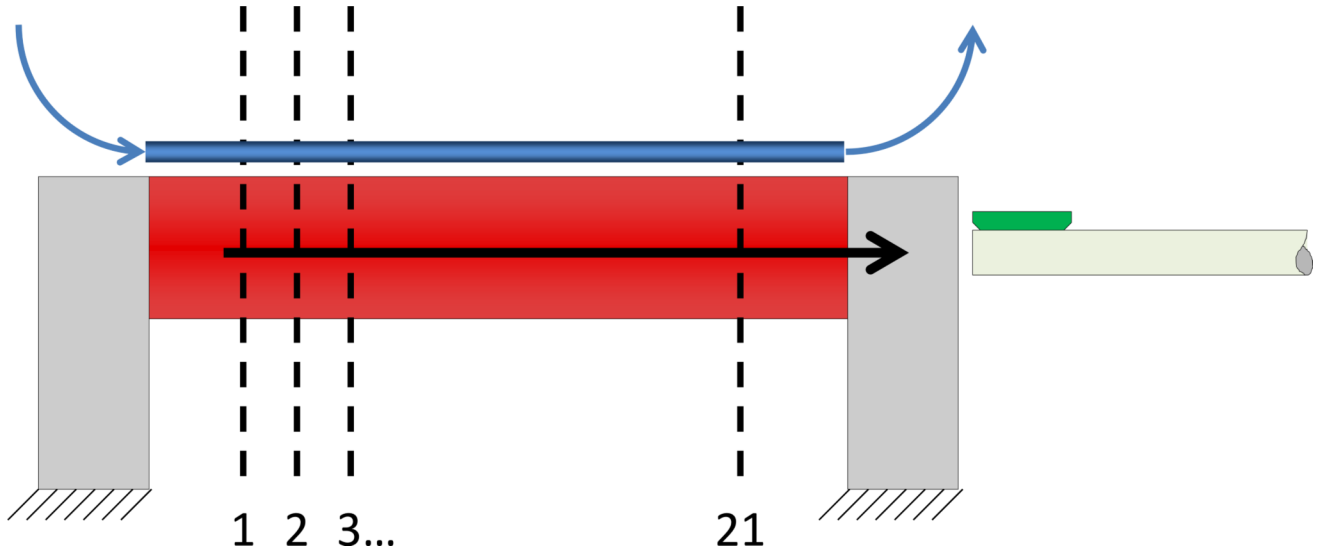
Figure 4.
Illustration of the *ex vivo* imaging setup. The porcine artery is sutured and attached to a custom fixture on either side that immobilizes the tissue during the imaging process. A 200 µm diameter microcellulose tube is placed outside of the artery to simulate a deep *vasa vasorum* vessel and contrast agents are flowed through the vessel at a fixed concentration. The transducer is placed within the lumen of the vessel and images are acquired in 21 different planes (dashed lines) separated by 200 µm under automated pullback. At each imaging plane, the transducer is rotated for one revolution to acquire an image before advancement to the next imaging plane.
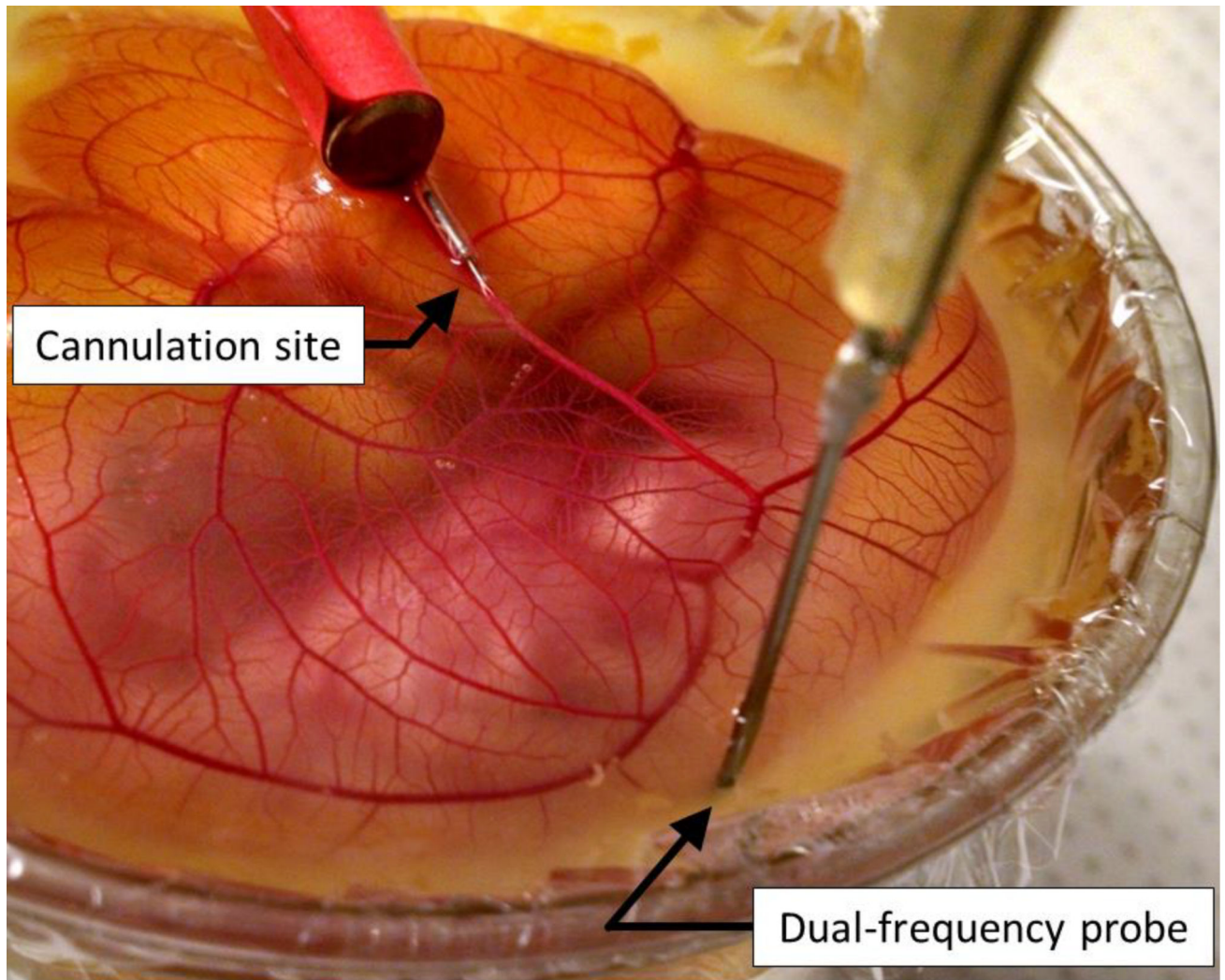
Figure 5.
Photograph illustrating the position used to acquire images from the chorioallantoic membrane.
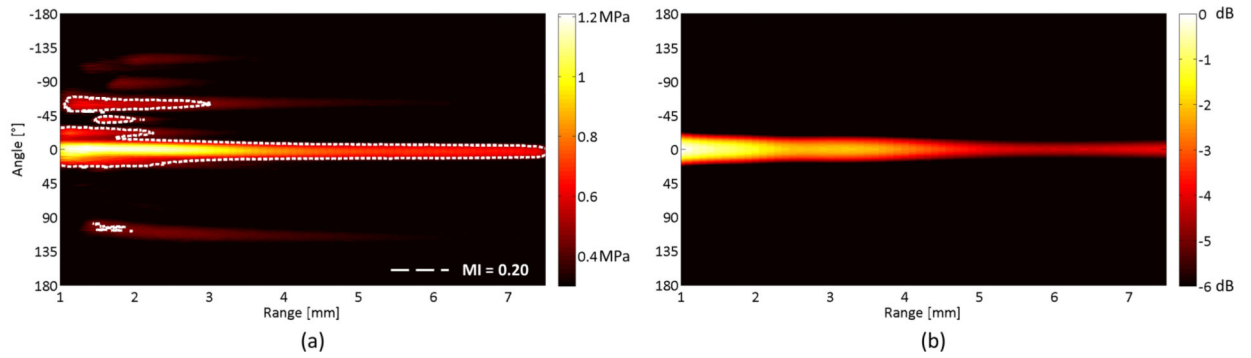
Figure 6.
(a) The measured pressure field distribution obtained by exciting the low frequency element with a Gaussian enveloped pulse and recording with a needle hydrophone. A dashed contour is overlaid on the field to identify the region having a mechanical index of 0.20 or higher which is the region containing the most nonlinear activity. (b) The simulated transmit pressure field using the impulse response from the low frequency element.
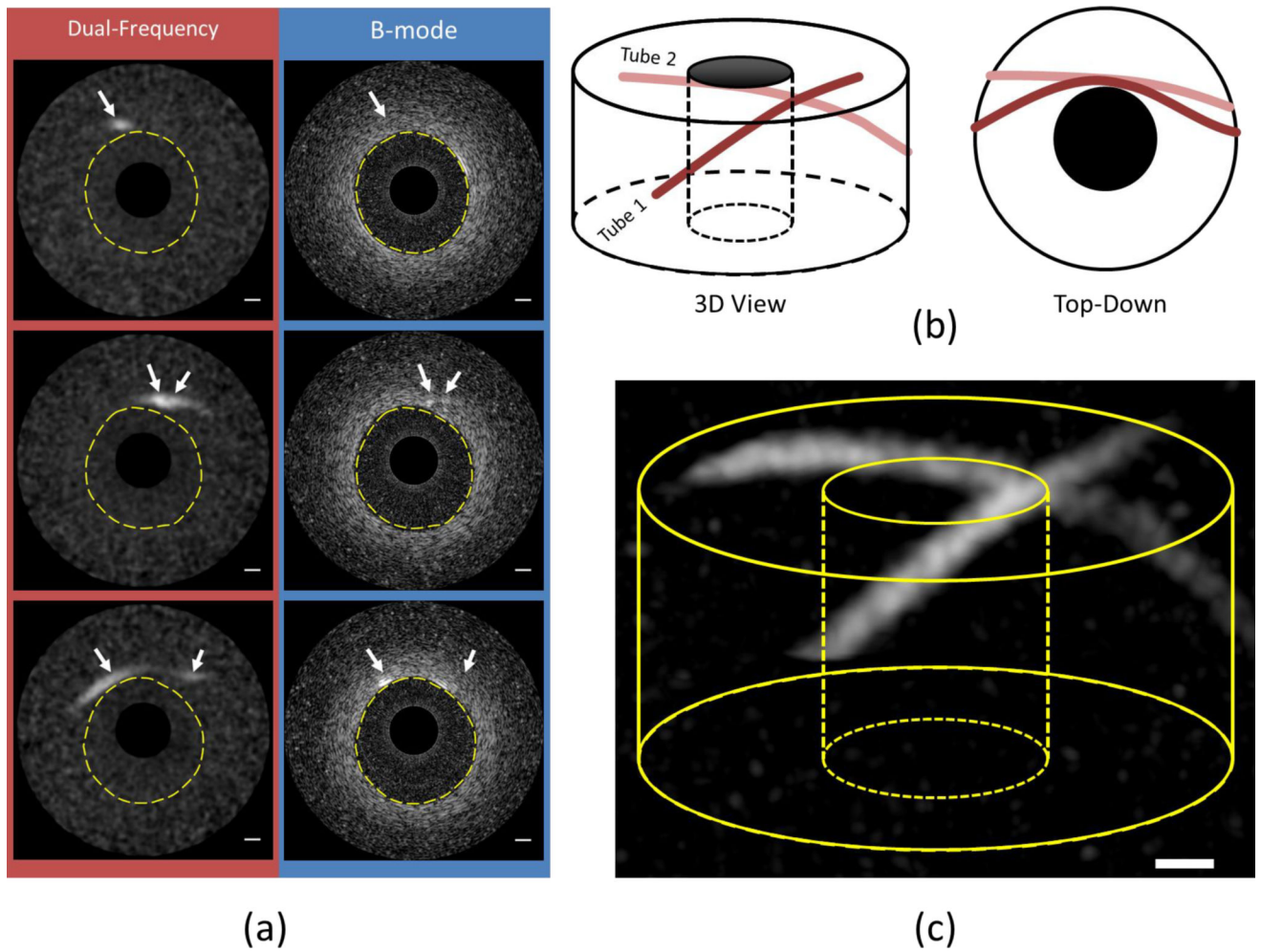
Figure 7.
(a) Cross sectional images of dual-frequency mode (left pane) and B-mode (right pane) show the presence of contrast agent (arrows) in a tissue mimicking phantom. The phantom lumen is outlined in both imaging modes for reference. (b) Cartoon illustrating the relative orientation of the contrast filled tubes embedded in the graphite phantom. (c) Three-dimensional rendering of DF contrast specific imaging highlight the location of contrast filled tubes embedded within the phantom. Scale bars correspond to 1 mm in all figures while DF images are displayed with a 10 dB dynamic range and 40 dB for B-mode.
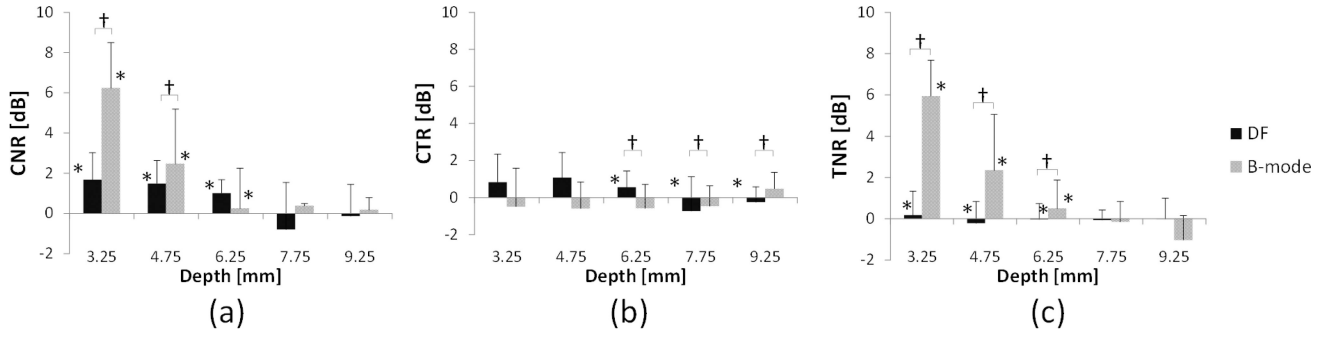
Figure 8.
Comparison of image metrics as a function of depth for both B-mode and dual-frequency mode contrast imaging. (a) Contrast-to-noise ratios using B-mode exceed those provided by DF mode, and at depths beyond 7 mm, the signal quality of both imaging modes fall below the noise floor giving CNR equal to zero. (b) Contrast-to-tissue ratios provide a measure of specificity of preferentially enhancing regions of contrast agents relative to surrounding tissue. DF mode images were non-zero and statistically higher than corresponding B-mode images. (c) The TNR of DF images were much lower than those found in B-mode, indicating that DF mode images are largely devoid of tissue backscatter. Asterisks (*) indicate that the mean is non-zero while daggers (†) show the means between groups are statistically different.
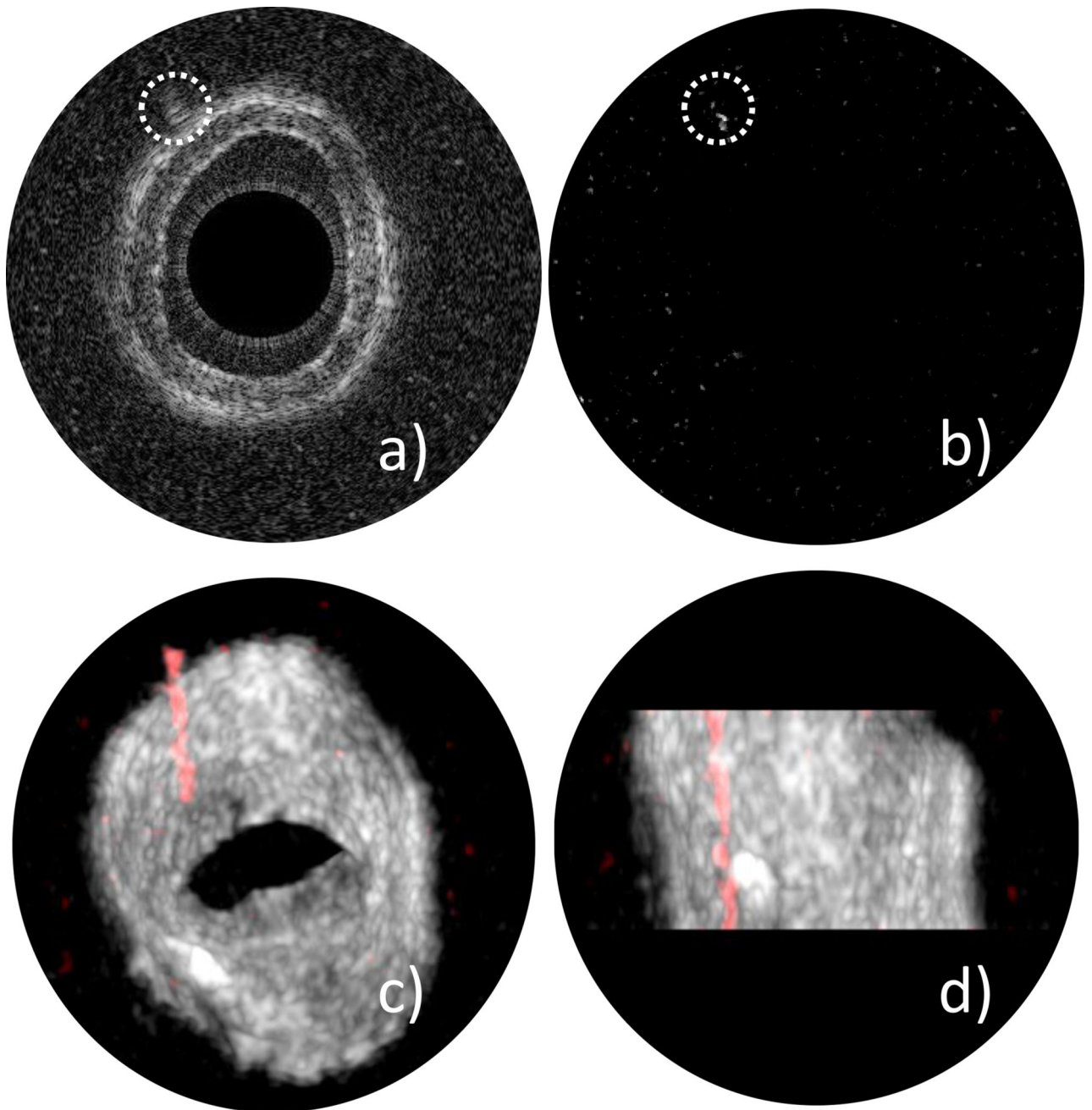
Figure 9.
Ex vivo imaging experiments through a porcine vessel using B-mode and dual-frequency contrast imaging show significant tissue reduction when operating in dual-frequency mode. (a) The B-mode image is acquired by placing the transducer within a suspended porcine coronary artery. The mean diameter of the lumen was measured to be 8.1 mm with a wall thickness of 1.42 mm. The dotted white circle indicates the location of the microcellulose tube placed external to the vessel. (b) A DF mode contrast image. Backscatter from tissue is largely suppressed while microbubble signal is still retained (dashed circle). (c) Orthotropic view and (d) side views of a 3D volume rendering of the vessel. Contrast signal (depicted in

red) was detected through the vessel and has been overlaid on traditional B-mode images (gray), showing the capability of the system to clearly identify the location of the 200 micron artificial microvessel.
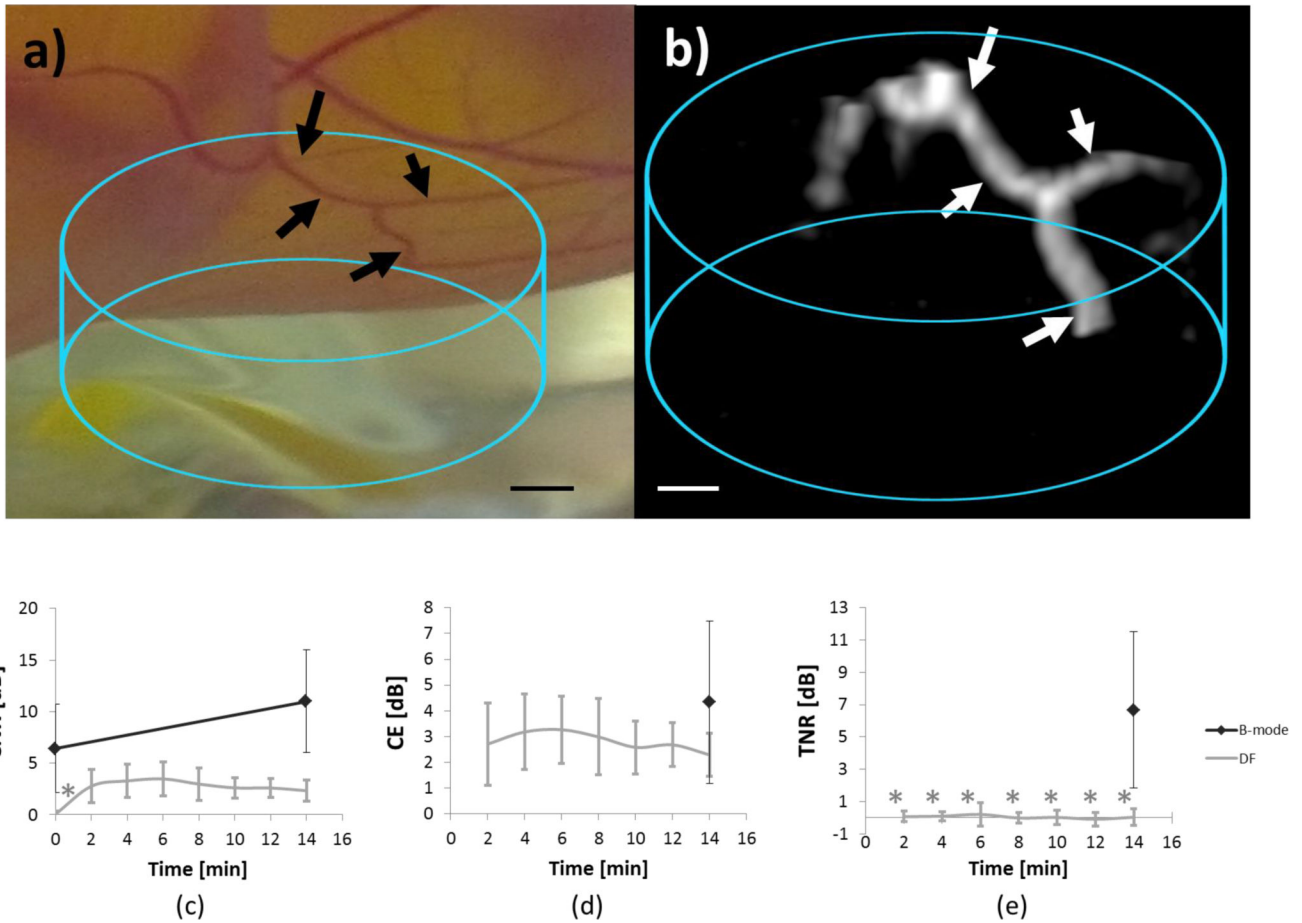
Figure 10.
(a) Photograph taken of the chorioallantoic membrane at 14 days showing microvasculature. The IVUS transducer was positioned relative to the vessels of interest (arrows) where a 4 mm pullback was performed (cylindrical outline). (b) Three dimensional contrast specific rendering of the same region photographed using the dual-frequency IVUS transducer. Fiduciary marks (arrows) are used to aid the reader in coregistration of the optical and ultrasound images. Scale bars correspond to 1 mm distance. (c) Contrast-to-noise ratios improved for either imaging mode after injection of MCAs, with B-mode images having larger CNRs compared to DF modes. (d) Contrast enhancement after 14 minutes of infusion was not statistically different between the imaging modes ($p = 0.07$). (e) Tissue-to-noise ratios at all time points were statistically zero for DF images, indicating this imaging mode is capable of suppressing tissue harmonics effectively. B-mode images had a mean tissue to noise ratio of 6.67 dB after contrast injection.